WILEY-VCH

DOI: 10.1002/ ((please add manuscript number))

Article type: Full Paper

Plasmonic Au/TiO_2-dumbbell-on-film nanocavities for high-efficiency hot-carrier generation and extraction

Kwun Hei Willis Ho,[1] Aixue Shang,[1] Fenghua Shi,[1] Tsz Wing Lo,[1] Pui Hong Yeung,[1] Yat Sing Yu,[1] Xuming Zhang,[1] Kwok-yin Wong,[2] Dang Yuan Lei[1]*

[1]Department of Applied Physics, The Hong Kong Polytechnic University, Hong Kong, China
[2]Department of Applied Biology and Chemical Technology, The Hong Kong Polytechnic University, Hong Kong, China

E-mail: dylei@polyu.edu.hk

Keywords: hot carriers; surface plasmons; particle-on-film nanocavities; Au/TiO_2 dumbbell nanostructures; visible-light photocatalysis

Abstract:

Plasmon-induced hot carriers have attracted intensive research attention due to their vast potential for light-triggered high-efficiency carrier generation and extraction, which can overcome the optical bandgap limit of conventional semiconductor-based optoelectronic devices. Here, we demonstrate that Au/TiO_2 dumbbell nanostructures assembled on a thin Au film serve as an efficient optical absorber and hot-carrier generator in the visible region. Upon excitation of localized surface plasmons in such coupled particle-on-film nanocavities, the energetic conduction electrons in Au can be injected over the Au/TiO_2 Schottky barrier and migrate to TiO_2, participating in the chemical reaction occurring at the TiO_2 surface. Compared with the same dumbbell nanostructures on an ITO film, the Au-film-coupled system exhibits remarkable enhancements in both photocurrent amplitude (more than one order of magnitude) and reaction rate (up to three times), which are mainly due to the plasmon resonance enhancement and near-field amplification in the presence of the Au film. The incident-wavelength-dependent photocurrent and reaction rate measurements jointly reveal that the Au-film-mediated near-field localization not only significantly facilitates more efficient electron-hole separation and transport in the coupled system but also promotes strong d-band optical transitions in

the film itself for generation of extra hot electrons. Our nanocavity system provides a new plasmonic platform for effective photoexcitation and extraction of hot carriers and also better understanding of their fundamental science and technological implications in solar energy harvesting.

1. Introduction

Plasmon-mediated photoexcitation of hot carriers has attracted an increasing research interest due to its wide potential applications in photovoltaics,[1-3] photodetection[4-5] and photocatalysis.[6-9] Unlike photoexcited carriers in semiconductors, the hot carriers stimulated in metals exhibit favourable excitation conditions by overcoming the bandgap limitation[10-12] and can directly participant in chemical reactions through charge transfer.[13-15] However, conventional hot-carrier devices suffer from inefficient excitation and extraction since strategies are seldom adopted to simultaneously enhance the optical absorption and hot-carrier transport, which consequently generates low photocurrents. By the means of collective oscillation of the conduction electrons in metallic nanostructures, hot-carrier generation can be remarkably promoted by invoking their surface plasmon resonance (SPR), which is regarded as one of the most effective ways for hot-carrier generation and extraction.

Various Au/TiO_2 nanostructures have been developed as novel metal-semiconductor hybrid platforms, which have been widely used in many applications by harnessing the localized SPR induced visible-light confinement and harvesting.[16-18] These nanostructures can be easily incorporated into optoelectronic devices and thus improve the visible-light responsivity. One type of such prevailing nanostructures is the Au/TiO_2 core/shell configuration in which the metallic core concentrates the far-field radiation into a sub-wavelength volume to locally generate plasmonic hot carriers that can subsequently transfer to the semiconducting shell. Note that the semiconductor shell also provides optical spacing,[19-20] chemical stability and electrical conductivity.[21] By varying core diameter and shell thickness, the plasmonic response of core/shell nanostructures can be flexibly tuned to meet the needs of specific applications.[22] Another interesting configuration is the Au-film/TiO_2-film/Au-

nanosphere sandwich system that has been used as a broadband visible-light absorber capable of efficiently converting the absorbed visible photon energy to plasmon-mediated photocurrent generation.[23-24] However, those subwavelength spherical nanoparticles support only one plasmon resonance mode that restricts the near-field strength amplification compared with metallic nanorods or nanocubes.[25] Besides, the critical role of the Au film in hot-carrier generation and separation when coupled with metallic nanoparticles remains unclear. Therefore, it is essential to comprehensively elucidate the plasmonic resonance properties and hot-carrier transfer mechanism in such coupled particle-on-film nanocavities.

In this study, we investigate the plasmonic response of Au/TiO_2-dumbbell-on-Au-film nanocavities and explore the physical mechanism of dumbbell-film coupling mediated hot-carrier generation and transfer at the two TiO_2-Au interfaces. In experiment, the dumbbell-shaped Au/TiO_2 nanoparticles were prepared by encapsulating the two ends of Au nanorods with TiO_2 shells, which were then self-assembled on two thin films, i.e. plasmonic Au and conducting ITO to form two systems with distinctively different optical and electrical properties. Optically, the Au/TiO_2-dumbbell-on-Au shows a strong film-mediated near-field localization and confinement compared with its counterpart on ITO, and therefore can locally generate hot carriers under visible-light illumination; Electrically, a Schottky barrier is established between the Au nanorod and TiO_2 shell to collect the hot electrons generated through non-radiative decay of the localized SPR excitation in both configurations, however, an additional Schottky barrier is electrically constructed at the TiO_2/Au-film interfacial contact, allowing the extraction of hot carriers from the photoexcited d-band transitions in the Au film. Although the hot-electron injections from the Au nanorod and the Au film to the TiO_2 shell in the coupled system apparently counter each other with reversed current direction, both sources of hot electrons facilitate the photocatalytic reaction at the TiO_2 shell surface, as manifested by an extraordinary performance in the dye decomposition experiment.

2. Results and discussion

2.1 Morphology characterization and working principle

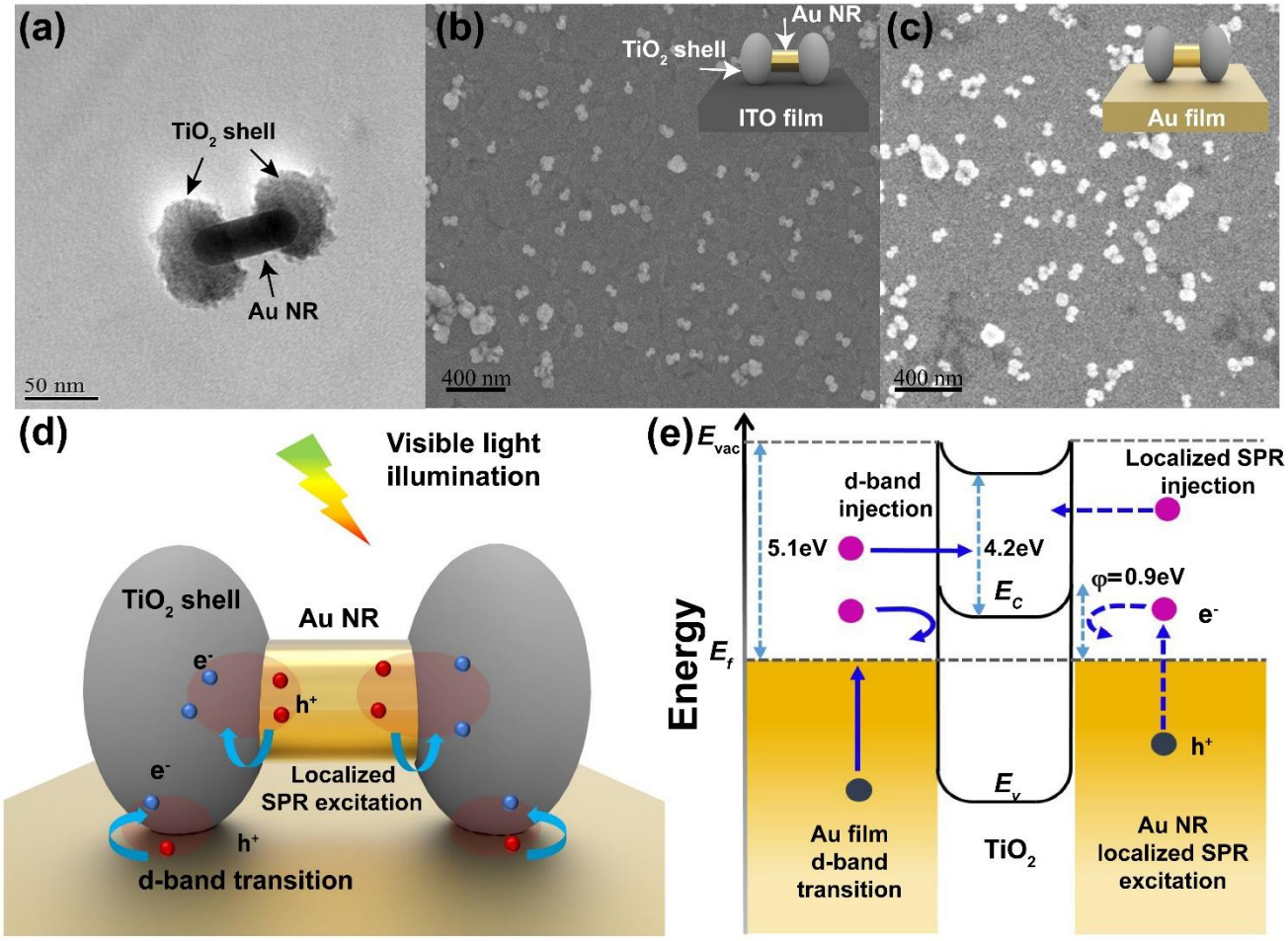

Figure 1. (a) TEM graph of a Au/TiO_2 dumbbell-shaped nanostructure captured at magnification of 50000X. (b, c) SEM images of Au/TiO_2 dumbbell nanostructures deposited on an ITO glass (b) and a thin Au film (c). (d) Pictorial sketch of the hot-carrier generation in a Au/TiO_2-dumbbell-on-Au-film nanocavity through both localized SPR excitation and d-band transitions. (e) Schematic band diagram for a Au/TiO_2-dumbbell-on-Au-film nanocavity, illustrating the pathways of hot-carrier excitation and injection. The work function of Au, Φ_{Au} = 5.1 eV, and affinity of TiO_2, χ = 4.2 eV, are indicated in the band digram.

We first introduce the Au/TiO_2 dumbbell-shaped nanostructures used in our study and discuss how to make uniform deposition of such nanostructures on substrates. The dumbbell nanostructures were synthesized with a wet-chemistry method[26] in which anisotropic TiO_2 shells were selectively grown at the two ends of Au nanorods by controlling the density of the surfactant – DTAB on the rod surface. The TEM graph in Figure 1(a) depicts a single Au/TiO_2 dumbbell nanoparticle prepared with our method, and the average size of Au nanorods is estimated to be 78 nm in length and 23 nm in diameter

(see Figure S1a-b for detailed statistics) and the average thickness of TiO_2 shells is about 31 nm (see Figure S1c). To obtain uniform deposition of Au/TiO_2 dumbbells on the two substrates, i.e. a thin Au film and an ITO glass, we carefully adjusted the speed of spin-coating to precisely control the surface density of deposited Au/TiO_2 dumbbells,[27] which can prevent unwanted nanoparticle-aggregation-induced plasmon coupling.[28] The TEM images shown in Figure 1(b) and (c) confirm uniform deposition of Au/TiO_2 dumbbells on both Au film and ITO glass, exhibiting better dispersion than that prepared with simple drop-casting (see Figure S2 for uniformity comparison of the two methods).

In the context of plasmon-assisted visible-light-driven photocatalysis, the Au/TiO_2 dumbbell nanostructures outperform Au@TiO_2 core-shell nanostructures due to efficient spatial separation of electron/hole pairs. The carrier generation and transport processes in the Au/TiO_2/Au nanocavity system are more interesting, as schematically illustrated in Figure 1d and physically described by the band diagram in Figure 1(e). For comparison, the band diagram for the Au/TiO_2/ITO system is shown in Figure S3. Specifically, hot carriers can be generated only through localized SPR excitation in the Au nanorod in the Au/TiO_2/ITO system; however, both localized SPR excitation in the Au nanorod and direct optical excitation of d-band transitions in the Au film can induce hot carriers in the Au/TiO_2/Au system as schematically illustrated in Figure 1(d). The dual-channel carrier generation mechanism associated with the Au/TiO_2/Au system leads to an intriguing carrier transport process. The two Au/TiO_2 Schottky junctions electrically established at the interfacial contact allow for injection of hot electrons to the conduction band of TiO_2 through two pathways with opposite photocurrent direction: 1) the hot electrons induced by the nonradiative plasmon damping in the Au nanorod can be injected into the TiO_2 shell,[29-31] which dominates the photocurrent generation of the whole system; 2) the Au film has optical d-band transitions at around 500 nm,[32,33] which also enables the migration of hot electrons to the TiO_2 conduction band. Such dual-channel hot-electron injection are illustrated in the proposed band diagram in Figure 1(e). In the following, we will experimentally

reveal the proposed hot carrier transport mechanism in the coupled plasmonic particle-on-film nanocavities by investigating their optical response and wavelength-dependent photocurrent.

2.2 Optical characterization

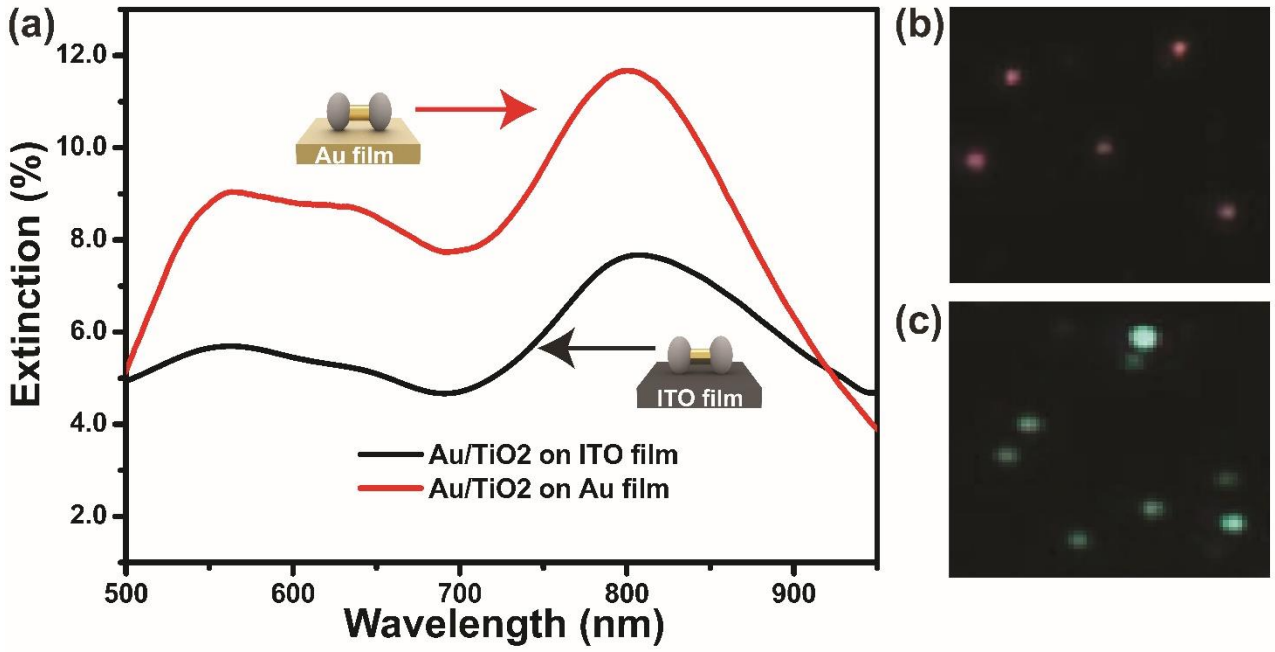

Figure 2. The optical response of Au/TiO_2 dumbbells on an ITO glass and on a thin Au film. (a) Extinction spectra of the Au/TiO_2 dumbbells on the ITO glass (black curve) and on the Au film (red curve) measured with a microscope system equipped with a 10X objective lens. (b, c) Optical dark-field microscope images of the Au/TiO_2 dumbbells on the ITO glass (b) and on the Au film (c). The dark-field images were obtained with the same microscope system with a 50X objective lens.

The optical properties of the Au/TiO_2/Au and Au/TiO_2/ITO systems were characterized by an optical microscope system (Olympus BX-51). The extinction of the two systems are defined as 1- *R* - *T*, where *T* is the transmittance of the systems and *R* is the reflectance. Since the Au film was sputtered on an opaque silicon wafer with zero transmittance, the extinction in the Au-film-coupled system is defined as 1 - *R*. By subtracting the background extinction of both ITO and Au film, we can extract the pure extinction of the Au/TiO_2 dumbbells on both substrates to compare their optical responses. When the Au/TiO_2 dumbbells are placed on a substrate, the anisotropic TiO_2 shells isolate the Au nanorods from the substrate, creating non-contact plasmonic nanocavities. The extinction of the Au/TiO_2 dumbbells assembled on the ITO glass has two distinct peaks at 560 and 820 nm,

corresponding to the transverse and longitudinal localized SPR resonance modes of the Au nanorods, respectively. In comparison, the dumbbells on the thin Au film show two peaks at 560 and 800 nm, with the longitudinal one narrower than that of the dumbbells on ITO. For the Au/TiO_2/ITO system, the full-width at half maximum (FWHM) of the longitudinal resonance is estimated to be ~160 nm, while it shrinks to ~130 nm for the Au/TiO_2/Au system. This is consistent with our pervious observation that a thin Au film can modulate the localized SPR mode of metallic nanoparticles on top, resulting in resonance linewidth shrinking.[34-35] Besides, it is also worthwhile to note that, in the Au/TiO_2/Au system, larger incidence angle associated with the 50X objective lens used in our experiment can enhance the extinction intensity at 560 nm, becoming comparable to the long-wavelength extinction peak (Figure S4). This observation is in good agreement with the dark-field images shown in Figure 2(b) and (c), where the Au/TiO_2 dumbbells appear reddish on the ITO film while greenish on the Au film, suggesting that the Au/TiO_2 dumbbells on ITO has a far-field scattering radiation dominated in the long-wavelength region and the short-wavelength scattering is enhanced when coupled to the Au film. The detailed optical responses of the two systems will be discussed later in connection with FDTD simulation results.

Compared to the ITO substrate system, the Au-film-coupled nanocavity provides an extra advantage associated with its unique configuration. In the long-wavelength region (>750 nm), the Au film has very high reflectance (~90%) (Figure S5), and thus it can serve as a rear mirror to reflect the incident light, further enhancing the extinction intensity of the Au/TiO_2 dumbbells as shown in Figure 2(a). While in the short-wavelength region (<600 nm), the reflectance is lowered due to the increased photon absorption by the Au film itself, which is originated from the optical d-band transitions under excitation by high-energy photons.

2.3 Electromagnetic Simulation

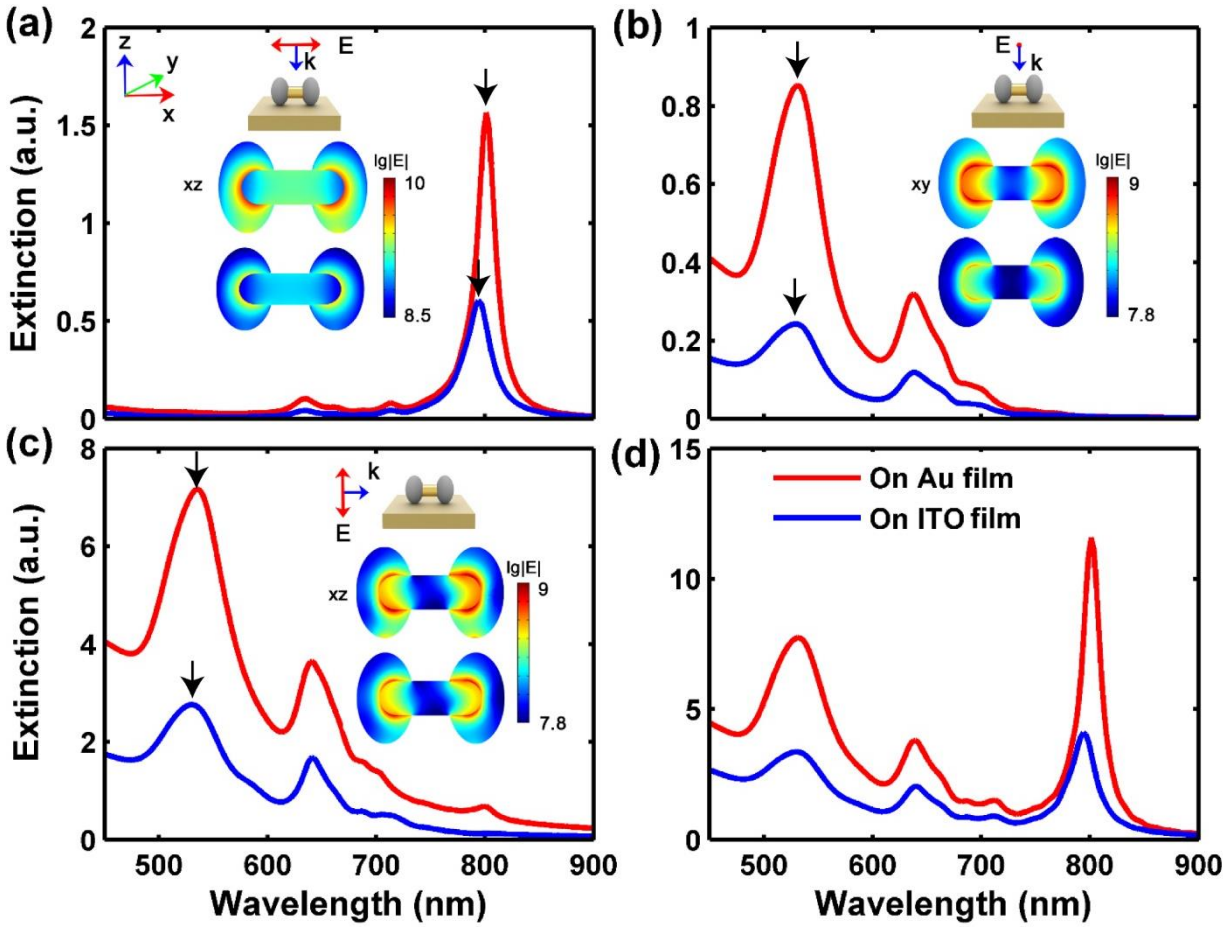

Figure 3. Simulated extinction spectra of a Au/TiO_2 dumbbell nanoparticle with experimentally determined geometrical dimensions on a 100 nm thick Au film (red lines) and on a semi-infinite ITO substrate (black lines): (a) the incident E-field is parallel to the *x*-axis (i.e. the long axis of the dumbbell) and (b) parallel to the *y*-axis (i.e. the short axis of the dumbbell) both under normal incidence; (c) the incident E-field is parallel to the *z*-axis (i.e. the short axis of the dumbbell under horizontal incidence). Each inset shows corresponding excitation configuration and simulated electric near-field distribution profiles at the resonance wavelengths as labelled by the arrows. (d) Simulated extinction spectra for randomly distributed Au/TiO_2 dumbbell nanoparticles on both substrates.

To have a comprehensive understanding on the optical response of the present structures and look deep into the resonance modes sustained by the two systems, we use the finite-difference-time-domain method implemented in the platform of Lumerical FDTD Solutions to investigate their extinction response and electric near-field distribution profile. On the one hand, the longitudinal and transverse resonance modes of the two systems are respectively studied in Figure 3(a) and (b), where the incident E-field is parallel to the long axis of the rod in Figure 3(a) and the short axis of the rod in Figure 3(b), both under normal incidence. The simulated extinction spectra for both systems show

two resonance modes, one long-wavelength peak at ~800 nm and the other short-wavelength peak at ~530 nm, which are ascribed to the longitudinal and transverse localized SPR of the Au/TiO_2 dumbbell, respectively. Compared to the Au/TiO_2 dumbbell on the ITO substrate, the longitudinal localized SPR of the Au-film-coupled nanocavity exhibits a linewidth shrinking: the FWHM of the 800 nm resonance peak is ~30 nm for the ITO-supporting system while it shrinks to ~19 nm for the Au-film-coupled system, a signature of plasmonic coupling between the Au/TiO_2 dumbbell and the Au film underneath. More importantly, we observe that the extinction intensity of the two resonance modes in the Au-film-coupled nanocavities are enhanced by 3-4 times compared to that for the Au/TiO_2 dumbbells on ITO, which is because the plasmonic coupling between the Au/TiO_2 dumbbell and the Au film underneath contributes an extra photon absorption channel.

Since in our experiment the two systems were illuminated with a focused white light beam by a 50X objective, consisting of a significant out-of-plane electric-field component (i.e., parallel to the *z*-axis), here we also simulate the extinction spectra for the two systems with field polarization along the *z*-axis and light propagation along the *x*-axis, with results shown in Figure 3(c). Similar to the observation in Figure 3(b), a remarkable extinction enhancement is found at the short-wavelength peak for the Au-film-coupled nanocavity system. Let us analyse these three illumination cases as illustrated in Figure 3(a-c). In Figure 3(a), the E-field is along the *x*-axis of the rod when the light is normal incident at the sample surface. This field component can effectively excite the longitudinal localized SPR mode (~800 nm). As the incident angle increases in the *x*-*z* plane, the E-field can be decomposed into two components, one along the *x*-axis and the other along the *z*-axis. In an extreme case (i.e. incident angle 90^o), the E-field is totally along the *z*-axis (see Figure 3(c)). On contrary, the E-field in Figure 3(b) is always along the *y*-axis, which is independent on the incident angle. The *z*- and *y*-axis E-field components can excite the same resonance mode (i.e. the transvers localized SPR mode at ~530 nm). In our experiment, the unpolarised illumination has all three cases. When the incident angle becomes larger, the E-field *z*-axis component increases as described above while the y-axis component preserves. Therefore, the extinction intensity at 560 nm can be enhanced at larger

incidence angles. Such far-field extinction enhancement is consistent with the simulated near-field results. As can be seen from the near-field distribution profiles in the insets of Figure 3(a) and (b), the near-field strength in the Au-film-coupled nanocavity is increased in magnitude and the field localization is stronger than the Au/TiO_2/ITO system.

After understanding those localized SPR modes in the two systems under specific excitation conditions, we construct a general model to simulate the extinction spectra of the Au/TiO_2 nano-dumbbells randomly distributed on the thin Au film and on ITO substrate, mimicking the exact experimental situation. The simulated extinction spectra for the two systems are shown in Figure 3(d), which agree well with the experimental results in Figure 2a (see Figure S6 for direct comparison), in terms of both peak position and extinction intensity. This agreement further confirms that both longitudinal and transverse localized SPR modes contribute to the total optical absorbance of the Au-film-coupled nanocavities. Note that spectral modulation of localized SPR modes has important implications in efficient hot-carrier generation and extraction. Since the non-radiative damping of localized surface plasmons is believed to result in hot-carrier generation, the near-field strength and distribution associated with the relevant plasmon modes would be crucial. Therefore, the Au-film-coupled nanocavity system is expected to have a much higher efficiency in generating plasmon-decay-induced hot carriers. In the coming paragraph, we will further discuss the hot-carrier generation behaviour in connection with the above-shown optical characterization and simulation results.

2.4 Photocurrent response over the visible-light region

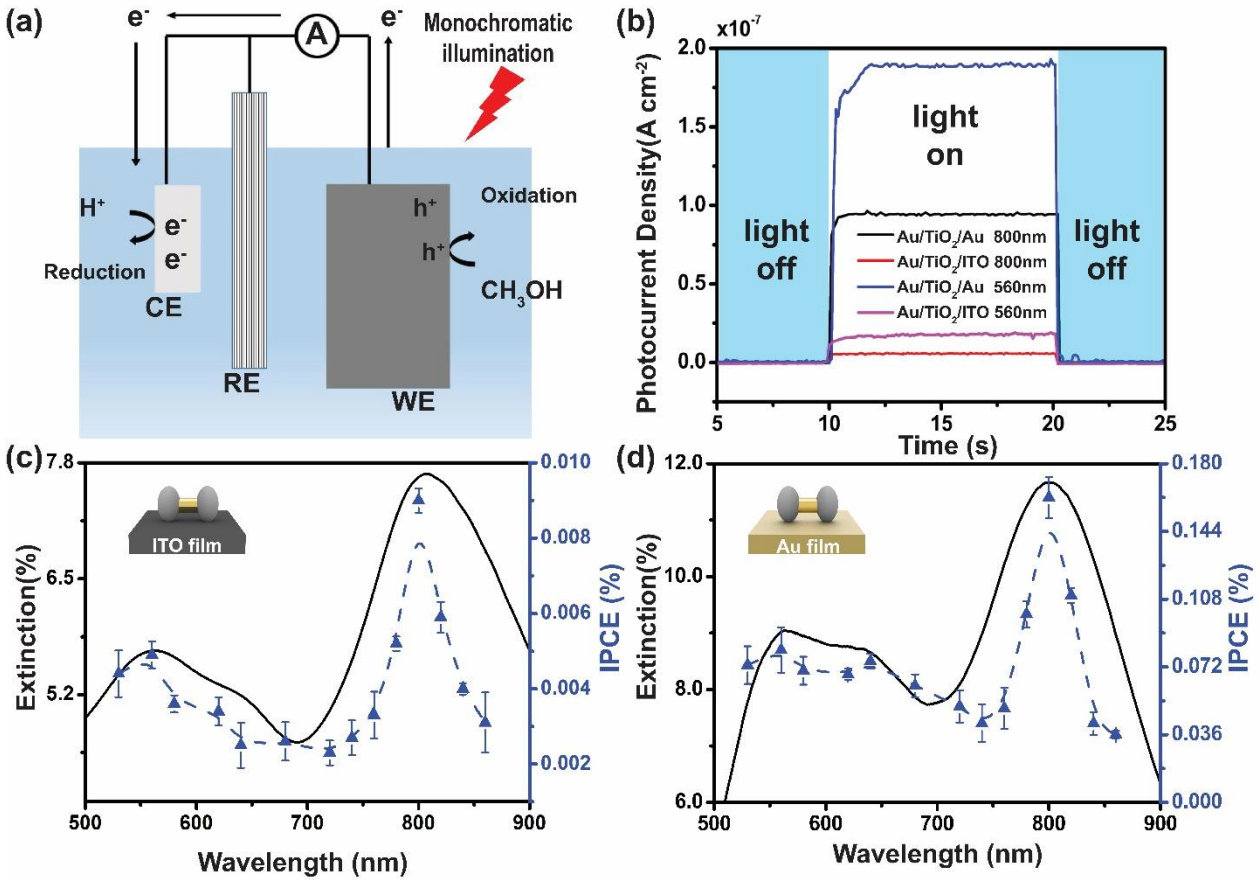

Figure 4. Wavelength-dependent photocurrent response of the Au/TiO_2/Au nanocavity and Au/TiO_2/ITO systems. (a) Sketch of the IPCE measurement setup used in our experiment. Here the plasmon-induced electron-hole pairs separate and the hot electrons transport from working electrode (WE) to counter electrode (CE). Satuarated Hg/Hg_2Cl_2 was used as reference electrode (RE). (b) Comparison of measured photocurrent under 800 nm (black: Au/TiO_2/Au, red: Au/TiO_2/ITO) and 560 nm (blue: Au/TiO_2/Au, magenta: Au/TiO_2/ITO) illumination. (c, d) Measured IPCE for the Au/TiO_2/ITO system (c) and the Au/TiO_2/Au nanocavity system (d), in comparison along with their corresponding extinction spectra. The error bars are standard deviation of three times measurements.

The photocurrent generation and transport in the two systems were measured with a three-electrode potentiostatic setup as shown in Figure 4(a). The nanoparticle density on the Au film and on the ITO substrate were inspected by our optical dark-field microscope system prior to photocurrent measurements. In Figure 4(a), the two plasmonic systems are respectively connected as working electrode in the measurement setup under illumination with a monochromatic light source. A Pt wire and saturated calomel (Hg/Hg_2Cl_2) serve as counter electrode and reference electrode, respectively, and the whole setup works in Na_2SO_4 electrolyte with 10% v/v methanol as sacrificial reagent.[36]

Based on the extinction peaks observed in Figure 2(a), we first study the photocurrent response of each plasmonic system under 560 and 800 nm illumination, respectively. The photocurrent results shown in Figure 4(b) suggest that the Au/TiO_2/Au nanocavity system has a remarkable photocurrent enhancement (more than ten-folds) compared to its counterpart, i.e. Au/TiO_2/ITO under both incident wavelengths at the same power. When the incident light is off, both plasmonic systems show negligible photocurrent, indicating little contribution of dark current in our setup.

To have a comprehensive comparison and depict the relative strength of photocurrent response of the two plasmonic systems, here we introduce the incident photon-to-electron conversion efficiency (IPCE), which is defined as:

$$\mathrm{IPCE} = \frac{1240}{\lambda(\mathrm{nm})} \times \frac{I_{\mathrm{m}}}{P_{\mathrm{in}}} \times 100\% \qquad (1)$$

where I_{m} (P_{in}) refers to the measured photocurrent density (incident light power density). The results in Figure 4(c) and (d) show that the wavelength-dependent IPCE for both systems follows the same trend as their extinction spectrum. To be specific, two IPCE peaks for the Au/TiO_2/ITO system are found at 560 and 800 nm as shown in Figure 4(c), which matches well with its extinction spectrum. To verify that the measured photocurrent is entirely from the localized SPR excitation of the Au/TiO_2 dumbbells, we measured a bare ITO substrate under the same illumination condition. As expected, no photocurrent was observed over the incident wavelength region, which corroborates that the photocurrent observed in our experiment is solely from the localized SPR excitation of the Au/TiO_2 dumbbells. Similarly, the IPCE curve for the Au/TiO_2/Au nanocavity system shown in Figure 4(d) is also found to have two peaks located at 560 and 800 nm, again in good agreement with its extinction spectrum. However, the two peaks show different IPCE magnitudes where the hot-carrier excitation in the long wavelength region is more efficient, consistent with their extinction intensity contrast. Remarkably, the IPCE values obtained for the Au/TiO_2/Au nanocavity system are nearly 15-fold larger than that for the Au/TiO_2/ITO at the same illumination wavelength of the same power. To explain this difference, we analyse the spatial distribution of electric near-field at the resonant

wavelengths observed in Figure 3(a) and (b), because it has been pointed out that the optical response such as field distribution, magnitude and localization in a plasmonic system is of critical importance for hot-carrier excitation and carrier transport.[8,37] In fact, the Schottky barrier height of the Au/TiO_2 junction is calculated to be ~0.9 eV as shown in the band diagram in Figure 1(e). Therefore, the hot-electron injection through plasmon damping is feasible for the whole excitation spectrum (580-860 nm). From the simulated field distribution profiles, we can see the following merits upon introducing the Au film in comparison with the ITO film. Firstly, the strength of electric near-field is significantly enhanced due to the near-field coupling between the dumbbell and the Au film, which ultimately results in a higher hot-carrier generation over the whole incidence spectrum. Secondly, the near-field distribution is much concentrated at the two ends of the dumbbell atop the Au film compared to the ITO glass, particularly at the long-wavelength peak, which dramatically increases the probability of the hot-electron injection into the nearby TiO_2 shell. Finally, the Au film servers as a rear reflector that allows the Au/TiO_2 dumbbell to collect more excitation photons by its localized SPR modes.

2.5 Carrier transport

In section 2.1, we have proposed that the Au/TiO_2/Au system generates hot carriers in dual channels. To verify this, we have fully exanimated the photocurrent generated in the Au/TiO_2/Au system. The short-wavelength photon illumination ($500<\lambda<560$ nm) induces no significant photocurrent (Figure S7) in the bare Au film due to inefficient hot-carrier collection without the presence of Schottky barrier. When pristine TiO_2 nanoparticles of 30 nm diameter are deposited on the Au film (TiO_2/Au), surprisingly, the system shows a negative photocurrent when the device is excited at the short-wavelength region ($500<\lambda<560$ nm, see Figure S7), indicating that the current flow direction is reversed compared to the localized-SPR-induced photocurrent. This could be understood by investigating the optical property of the Au film: the reflection spectrum shown in Figure S5 indicates that the Au film has an increased extinction in the short-wavelength region (<580 nm), which is due to the optical transitions of electrons from the d-band to sp-band of Au. The photoexcited electrons

in the sp-band have a higher energy level than the TiO_2 conduction band,[38] thus the electron injection from the Au film to the TiO_2 shell is allowed. However, previous studies have suggested that the excited d-band electrons in a Au nanorod can non-radiatively decay into its localized SPR band, providing an extra channel for the relaxation of the excited d-band electrons.[39] Note that the hot carrier generation is also sensitive to structure geometry, particularly for Au nanostructures with dimensions or Au films with thickness smaller than 10 nm.[40] By considering the whole Au/TiO_2/Au system, it is obvious that hot electrons generated by the localized surface plasmons in the Au nanorod and by the optical d-band transitions in the Au film are both injected into the TiO_2 conduction band, yet in opposite directions. Although the reversed current direction weakens the measured IPCE magnitude, such dual-channel injection of hot electrons into the TiO_2 conduction band make the Au/TiO_2/Au system an excellent plasmonic photocatalysis platform since photocatalytic reactions take places at the TiO_2 surface.[41]

2.6 Photocatalytic organic decomposition

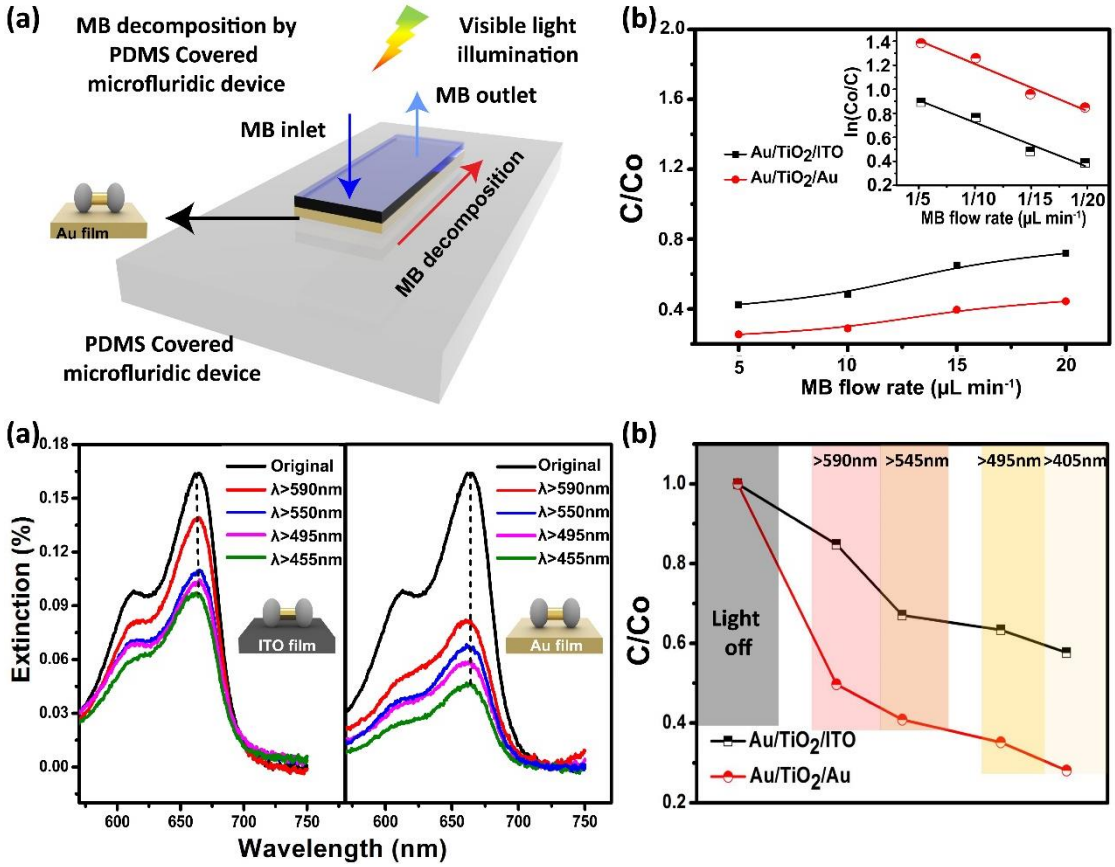

Figure 5. Photocatalytic decomposition of Methylene blue (MB) in a microfluidic device. (a) Sketch of microfluidic device for the MB decomposition experiment: The Au/TiO_2/ITO and Au/TiO_2/Au systems are respectively assembled in the device with a small cavity for flowing of MB. (b) Measured MB decomposition rate for the Au/TiO_2/ITO-based device (black curve) and the Au/TiO_2/Au-based device (red curve) both under >550 nm illumination. Insert shows the same data in logarithm scale. (c) Measured extinction spectra of the MB solution flowing through the two devices at flow rate of 10 μL·min^{-1} under different illumination spectra. (d) Extracted MB decomposition rate for the two devices under different illumination spectra.

To prove the Au/TiO_2/Au system exhibiting better photocatalytic activity over the visible light region, we perform a methylene blue (MB) decomposition experiment in a microfluidic device. The Au/TiO_2 nano-dumbbells on the ITO substrate and the thin Au film with similar nanoparticle density are respectively assembled inside two microfluidic devices covered with PDMS. In each device, a small cavity with 0.2 mm height is used as a flow pathway as shown in Figure 5(a). In the MB decomposition experiment, we used four long-pass filters to observe the decomposition rate as a function of illumination spectrum. As can be seen from Figure 5(b), under the visible-light illumination (filter >550 nm), the MB solution in the Au/TiO_2/Au-based system exhibits a higher decomposition efficiency than the Au/TiO_2/ITO-based system under varied flow rate. At the slowest flow rate (5 μL·min^{-1}), the Au/TiO_2/Au-based device reaches a decomposition rate C/Co equal to 0.26. The logarithm-scale plot of the measured decomposition rate shows a linear relationship to the inversed flow rate, demonstrating that the photocatalytic decomposition of MB follows a first-order kinetics.[42] Here decomposition of MB is initiated by the generation of hydroxyl radical ($OH^{\bullet}$) and superoxide radical ($O_2^{\bullet-}$).[43] When the Au/TiO_2/Au-based device is under visible-light illumination, no electron-hole pair is excited in TiO_2 (band gap ~3.2 eV). Therefore, we consider the radical generation originated from the excitation of hot carriers induced in the plasmonic nanocavities. The hot electrons generated from both d-band transitions and localized SPR excitation are injected to the conduction band of TiO_2 to produce $O_2^{\bullet-}$ radicals. On the other hand, the $OH^{\bullet}$ radicals are produced on the surface on both Au film and Au nanorods, where the hot holes with sufficient negative energy take part in the oxidization reaction.[44] The radical generation pathways are summarized below:

through the localized SPR-induced hot-carrier pathway:

$$h\nu + Au/TiO_2 \text{ dumbbell} \rightarrow (h^+)Au / (e^-)TiO_2$$

$$(h^+)Au + H_2O \rightarrow OH^\bullet + Au$$

$$(e^-)TiO_2 + O_2 \rightarrow TiO_2 + O_2^{\bullet-}$$

through the d-band transition induced hot-carrier pathway:

$$h\nu + TiO_2/Au \text{ film} \rightarrow (e^-)TiO_2 / (h^+)Au$$

$$(h^+)Au + H_2O \rightarrow OH^\bullet + Au$$

$$(e^-)TiO_2 + O_2 \rightarrow TiO_2 + O_2^{\bullet-}$$

From the pathways described above, we can see that both Au nanorods and Au film act as photoanode where the hot holes induce the formation of $OH^\bullet$ radicals while the TiO_2 shell acts as photocathode where the hot electrons induce the formation of $O_2^{\bullet-}$ radicals. The photocatalytic performance of both systems can be understood by the aforementioned spectrum-dependent analysis, which indicates that the MB concentration continuously decreases with increasing the illumination spectral range as shown in Figure 5(c). We also observe that the Au/TiO_2/Au-based device is more active in the short-wavelength region than the Au/TiO_2/ITO-based device. Such comparison further confirms the dual-channel hot-carrier generation in the former device. In the long-wavelength region (filter >590 nm), the MB decomposition mostly relies on the electron-pair generated by the longitudinal localized SPR of the Au/TiO_2 nano-dumbbells; However, in the short wavelength region (filter >550 nm), the decomposition is also facilitated by the optical transitions of d-band electrons in the Au film (although the decomposition is mainly contributed by the plasmon-induced hot electrons). As the illumination spectrum contains more short-wavelength photons (filters >495 nm and >450 nm), more electrons from the d-band transitions are injected to TiO_2, consistent with the strong absorption of Au at about 500 nm, which accelerates the MB decomposition in the short-wavelength region.

To further confirm the visible-light-driven photocatalytic decomposition of MB is resulted from the plasmonic hot carriers, we have conducted a set of control experiments by illuminating the same microfluidic devices without the deposition of Au/TiO_2 dumbbells. The results in Figure S10 clearly

show that in the absence of Au/TiO_2 dumbbells, the MB decomposition is not significant and has no wavelength dependence. The wavelength-dependent action spectra shown in Figure S11 also depicts the photocatalytic performance of the two devices. For the Au/TiO_2/ITO-based device, the apparent quantum yield (AQE) well matches the corresponding IPCE and extinction spectrum, with two peaks located at the two localized SPR bands (~560 and 800 nm). In contrast, the AQE for the Au/TiO_2/Au-based device is substantially higher than that for the Au/TiO_2/ITO-based device (~3 times enhancement), and it also follows the extinction and IPCE spectra in the long-wavelength region (>700 nm). In the short-wavelength region (<550 nm), the AQE for the Au/TiO_2/Au-based device slight deviates from the extinction and IPCE spectra. This observation is coherent with the spectrum-dependent analysis and the electron injection model proposed earlier: The photocurrent induced by the optical d-band transitions has a reversed direction to the plasmon-induced photocurrent, but in the photocatalytic decomposition experiment the hot electrons generated through both the d-band transitions and the localized SPR excitations simultaneously participant in the reactions.

3. Conclusion

In this work, we have synthesized Au/TiO_2 dumbbell nanoparticles in wet-chemistry environment and uniformly deposited the nano-dumbbells on ITO substrate and a thin Au film. With the aid of optical characterization and electromagnetic simulation, we show that the Au-film-coupled Au/TiO_2 dumbbells form plasmonic nanocavities with strong near-field localization and enhancement, which ultimately contributes to improved photocurrent generation and photocatalytic decomposition rate. Distinctly different from the ITO substrate based device, the Au-film-coupled dumbbells electrically form two Schottky junctions for plasmonic hot-carrier injection. Plasmon-induced hot carriers in the Au/TiO_2 dumbbell and the d-band transition induced hot carriers in the Au film simultaneously migrate through junction barrier and transport to the conduction band of TiO_2, resulting in photocurrents in opposite directions. Wavelength-dependent IPCE measurements and organic decomposition experiments furtherly verify that the Au/TiO_2 dumbbells assembled on the thin Au

film is more efficient in hot-carrier generation and collection. Although the d-band transitions contribute a reversed photocurrent that counters the localized SRP induced photocurrent, the electron injection serves as an additional channel that enhances the photocatalysis performance. Our study is beneficial to the basic understanding of plasmon-induced hot carriers and provides a new platform for high-efficiency hot-carrier generation and extraction.

4. Experimental section

Materials: Hexadecyltrimethylammonium bromide (CTAB >99%), Dodecyltrimethylammonium bromide (DTAB, >98%), Tetrachloroauric (III) acid ($HAuCl_4$), Sodium borohydride ($NaBH_4$ >99%), Silver nitrate ($AgNO_3$ >99%), Hydrochloric acid (HCl 1M), Ascorbic acid (AA >99%), Sodium bicarbonate ($NaHCO_3$ >99%), Titanium (III) chloride solution ($TiCl_3$, 15-20%, in 30% HCl solution), Methanol (CH_3OH >99%)and Sodium Sulphate (Na_2SO_4 >99%). All materials were brought from Sigma without further purification.

Synthesis of Au nanorods: Au nanorods were synthesized by a seed-medicated wet-chemistry method. A seed solution was prepared by mixing 9.75 mL CTAB (0.1 M) with 250 μL $HAuCl_4$ (10 mM), and 600 μL ice-cold $NaBH_4$ (10 mM) was then quickly added to the mixture. The resultant mixture was kept until the solution turned brownish, and then left undisturbed for 2 h. To prepare the growth solution, 42.5 mL CTAB (0.1 M) was added with 400 μL $AgNO_3$ (10 mM), 800 μL HCl (1 M) and 320 μL AA (1 M), followed by a rapid mixing until it turns to colourless. Finally, 150 μL as-prepared seed solution was added into the growth solution, with the final mixture left undisturbed overnight before further usage.

Synthesis of TiO_2/Au dumbbell nanoparticles: The synthesis procedures for Au/TiO_2 dumbbell nanoparticles follow the method reported by Wu *et al*.[26] 10 mL as-prepared Au nanorod solution was centrifuged twice (5500 rpm) and then re-dispersed into 2 mL DTAB (0.2 M) and 7.6 mL DI water. The resultant solution was left at room temperature for 1 h to allow uniform absorption of DTAB on the Au nanorods. The growth of anisotropic TiO_2 shells was initiated by $TiCl_3$ hydrolysis.

Typically, 400 μL $TiCl_3$ (15-20% $TiCl_3$ in 30% HCl) was diluted into 8 mL DI water and $NaHCO_3$ (1 M) was then added to adjust the solution pH value. The resultant TiO_2 shell thickness depends on the environment pH value. Adding 5 mL $NaHCO_3$ (1 M) turned the $TiCl_3$ solution into dark-blue and resulted in about 20-30 nm thick TiO_2 shells at the tips of Au nanorods. The as-prepared Au nanorod solution was immediately added into the dark-blue $TiCl_3$ solution and the mixture was kept under stirring for 15 min. To wash the unreacted titania precursor, the resultant Au/TiO_2 dumbbell solution was centrifuged twice (4500 rpm) then and then re-dispersed into 10 mL ethanol for further usage.

Spin-coating of Au/TiO_2 dumbbells on ITO and Au film: 400 μL concentrated Au/TiO_2 dumbbell solution was under sonication for 45 min and then dropped onto an ITO glass or a thin Au film (substrate size: 1 cm x 1.5 cm). After keeping the samples for 2 min to further increase the particle concentration, spin-coating at 2300 rpm was run for 20 s for the ITO substrate and at 1500 rpm for 10 s for the Au film sample.

Material characterization:

Electron microscope characterization: The geometry of Au/TiO_2 dumbbell nanoparticles was characterized by transmission electron microscope (JEOL-2011) working at 20 kV. The particle density of two plasmonic systems (Au/TiO_2/ITO and Au/TiO_2/Au) were inspected by scanning electron microscope (JEOL JSM-6335F) working at 12 kV.

Extinction characterization: Extinction spectra were obtained by reflectance (R) and transmittance (T) measurements in an optical microscope system (Olympics BX-150) equipped with 10X (N.A. 0.3) and 50 X objective (N.A. 0.5). Extinction spectra of Au/TiO_2 dumbbells were calculated as $1–R–T$ for the ITO sample and as $1–R$ for the Au film sample.

Incident photon-to-electron conversion efficiency (IPCE) measurements: The Au/TiO_2/ITO and Au/TiO_2/Au plasmonic systems were spin-coated with Nafion solution (5% v/v). Each system was then connected as working electrode in a three-electrode potentiostatic system with a Pt plate as counter electrode and Hg/Hg_2Cl_2 in saturated 4M KCl as reference electrode. All electrodes were immersed into 1M Na_2SO_4 solution with addition of 10% v/v methanol severing as sacrificial reagent.

Prior to light illumination, the electrolyte solution was purged with N_2 for 15 min. The working electrode was the illuminated through a quartz window with a 150 W Xeon lamp source that had a cut-off wavelength at 420 nm by a long-pass filter. For wavelength-dependent IPCE measurements, 15 band-pass filters with 15 nm bandwidth were used for spectral selection with centre wavelengths at 500 nm, 530 nm, 560 nm, 600 nm, 620 nm, 640 nm, 680 nm, 720 nm, 740 nm, 760 nm, 780 nm, 800 nm, 820 nm, 840 nm and 860 nm. Incident power was measured by a hand-held power meter (Thorlabs PM100).

Methylene blue (MB) decomposition: The Au/TiO_2/ITO and Au/TiO_2/Au plasmonic systems were respectively assembled inside a PDMS-covered microfluidic reactor. In the reactor, the Au/TiO_2 film was illuminated through the transparent PDMS cover while the MB solution (10^{-3} mM) passes through the microcavity of the reactor. To control the flow rate, a steady syringe pump was equipped in the microfluidic system, allowing four flow rates at 5, 10, 15 and 20 μL min^{-1}. Prior to light illumination, dark absorption was conducted when MB flowing at constant rate (5μL min^{-1}) for 15 min. After the dark absorption, the whole microfluidic device was illuminated by a 150 W Xeon lamp, and the illumination spectrum was selected by inserting four long-pass filters (>450 nm, >495 nm, >545 nm and >595 nm). Finally, the MB decomposition rate was characterized by measuring its concentration using a UV-Vis spectrometer with water as reference sample (Shimadzu Scientific Instruments, UV2550).

Supporting Information

Supporting Information is available from the Wiley Online Library or from the author.

Acknowledgements

We acknowledge the financial support by the Hong Kong Research Grants Council (ECS Grant No. 509513) and the Hong Kong Polytechnic University (Grant No. 1-ZVGH and 1-ZVH9).

Received: ((will be filled in by the editorial staff))
Revised: ((will be filled in by the editorial staff))
Published online: ((will be filled in by the editorial staff))

Reference

[1] J. Li, S. K. Cushing, F. Meng, T. R. Senty, A. D. Bristow, N. Wu, *Nat. Photonics* **2015**, 9, 601.

[2] S. Asahi, H. Teranishi, K. Kusaki, T. Kaizu, T. Kita, *Nat. Commun.* **2017**, 8, 14962.

[3] D. J. Farrell, H. Sodabanlu, Y. Wang, M. Sugiyama, Y. Okada, *Nat. Commun*. **2015**, 6, 8685.

[4] A. Pescaglini, A. Martin, D. Cammi, G. Juska, C. Ronning, E. Pelucchi, D. Iacopino, *Nano. Lett.* **2014**, 14, 6202.

[5] M. W. Knight, H. Sobhani, P. Nordlander, N. J. Halas, *Science* **2011**, 332, 702.

[6] Y. G. Wang, D. C. Cantu, M. S. Lee, J. Li, V. A. Glezakou, R. Rousseau, *J. Am. Chem. Soc.* **2016**, 138, 10467.

[7] L. Zhou, C. Zhang, M. J. McClain, A. Manjavacas, C. M. Krauter, S. Tian, F. Berg, H. O. Everitt, E. A. Carter, P. Nordlander, N. J. Halas, *Nano. Lett.* **2016**, 16, 1478.

[8] M. L. Brongersma, N. J. Halas, P. Nordlander, *Nat. Nanotech.* **2015**, 10, 25.

[9] Z. G. Dai, X.H. Xiao, W.Wu, Y.P, Zhang, L. Liao, S. S. Guo, J. J. Ying, C.X. Shan, M.T. Sun, C.Z. Jiang, *Light-Sci. Appl.* **2015**, 4, e342;

[10] K. Wu, J. Chen, J. R. McBride,T. Lian, *Science* 2015, 349, 6248.

[11] K. Wu, W. E. Rodriguez-Cordoba, Y. Yang, T. Lian, *Nano. Lett.* **2013**, 13, 5255.

[12] X. C. Ma, Y. Dai, L. Yu, B. B. Huang, *Light-Sci. Appl.* **2016**, 5, e16017.

[13] S. Linic, U. Aslam, C. Boerigter, M. Morabito, *Nat. Mater.* **2015**, 14, 567.

[14] Z. W. Seh, S. Liu, M. Low, S. Y. Zhang, Z. Liu, A. Mlayah, M. Y. Han, *Adv. Mater.* **2012**, 24, 2310.

[15] N. Zhou, L. Polavarapu, N. Gao, Y. Pan, P. Yuan, Q. Wang, Q. H. Xu, *Nanoscale* **2013**, 5, 4236.

[16] A. Ayati, A. Ahmadpour, F. F. Bamoharram, B. Tanhaei, M. Manttari, M. Sillanpaa, *Chemosphere* **2014**, 107, 163.

[17] Y. Tian, T. Tatsuma, *Chem. Commun* **2004**,0, 1810-1811

[18] Q. Sun, K. Ueno1, H. Yu, A. Kubo, Y. Matsuo,H. Misawa, *Light-Sci. Appl*. **2013,** 2, e118.

[19] F. Kang, J. He, T. Sun, Z. Y. Bao, F. Wang, D. Y. Lei, *Adv. Funct. Mater.* **2017**, 27.

[20] J. J. He, W. Zheng, F. Ligmajer, C.-F. Chan, Z. Y. Bao, K.-L. Wong, X. Y. Chen, J. H. Hao, J. Y. Dai, S.-F. Yu, D. Y. Lei, *Light-Sci. Appl*. **2017,** 6, e16217.

[21] H. L. Ding, Y. X. Zhang, S. Wang, J. M. Xu, S. C. Xu, and G. H. Li, *Chem. Mater.* **2012**, 24, 4572–4580

[22] C. Fang, H. Jia, S. Chang, Q. Ruan, P. Wang, T. Chen, J. Wang, *Energy Environ. Sci.* **2014**, 7, 3431.

[23] F. Tan, N. Wang, D. Y. Lei, W. Yu, X. Zhang, *Adv. Opt. Mater.* **2017**, 5.

[24] C. Ng, J. J. Cadusch, S. Dligatch, A. Roberts, T. J. Davis, P. Mulvaney, D. E. Gomez, *ACS Nano* **2016**, 10, 4704.

[25] H. Chen, L. Shao, Q. Li, J. Wang, *Chem. Soc. Rev*. **2013**, 42, 2679.

[26] B. Wu, D. Liu, S. Mubeen, T. T. Chuong, M. Moskovits, G. D. Stucky, *J. Am. Chem. Soc.* **2016**, 138, 1114.

[27] Y.-K. Hong, H. Kim, G. Lee, W. Kim, J.-I. Park, J. Cheon, J.-Y. Koo, *Appl. Phys. Lett.* **2002**, 80, 844.

[28] L. Shao, Q. Ruan, R. Jiang, J. Wang, *Small* **2014**, 10, 802.

[29] Y.L. Si, S. Cao, Z. Wu, Y. L. Ji, Y. Mi, X. Wu, X. F. Liu, L. G. Piao. *Appl. Catal. B* **2018**, 220, 471

[30] A.Giugni A, B.Torre, M. Allione, G. Das, Z. Wang, X. He, HN. Alshareef, E. Di Fabrizio, *Adv. Opt. Mater*. **2017**, 15,5

[31] A. Giugni,B. Torre, A. Toma, M. Francardi, M. Malerba, A. Alabastri, R.P. Zaccaria, M.I. Stockman, E. Di Fabrizio, *Nat. Nanotechnol*. **2013**,11, 845.
[32] M.-L. Thèye, *Phys. Rev. B* **1970**, 2, 3060.
[33] A. D. Rakic, A. B. Djurisic, J. M. Elazar, M. L. Majewski, *Appl. Opt.* **1998**, 37, 22
[34] G. C. Li, Y. L. Zhang, J. Jiang, Y. Luo, D. Y. Lei, *ACS Nano* **2017**, 11, 3067.
[35] G. C. Li, Y. L. Zhang, D. Y. Lei, *Nanoscale* **2016**, 8, 7119.
[36] A. Galinska, J. Walendziewski, *Energy & Fuels* **2005,** 19, 1143
[37] A. Manjavacas, J. G. Liu, V. Kulkarni,P. Nordlander, ACS Nano **2014**, 8, 7630
[38] H. Chen, G. Liu, L. Wang, *Sci. Rep.* **2015**, 5, 10852.
[39] A. Wan, T. Wang, T. Yin, A. Li, H. Hu, S. Li,ZX Shen,CA. Nijhuis, *ACS Photonics*, **2015**, 2, 1348.
[40] R. Sundararaman,P Narang,A.S. Jermyn,W.A. Goddard III, H.A. Atwater, *Nat. Commun*. **2014**, 16, 5788.
[41] C. Clavero, *Nat. Photonics* **2014**, 8, 95.
[42] N. Kannan, M. M.Sundaram, *Dyes. Pigm.* 2001, 51, 25.
[43] A. Houas, H. Lachheb, M. Ksibi, E. Elaloui, C. Guillard, J. M. Herrmann, *Appl. Catal., B* 2001, 31, 145.
[44] A. E. Schlather, A. Manjavacas, A. Lauchner, V. S. Marangoni, C. J. DeSantis, P. Nordlander, N. J. Halas, *J. Phys. Chem. Lett.* **2017**, 8, 2060.

Table of content

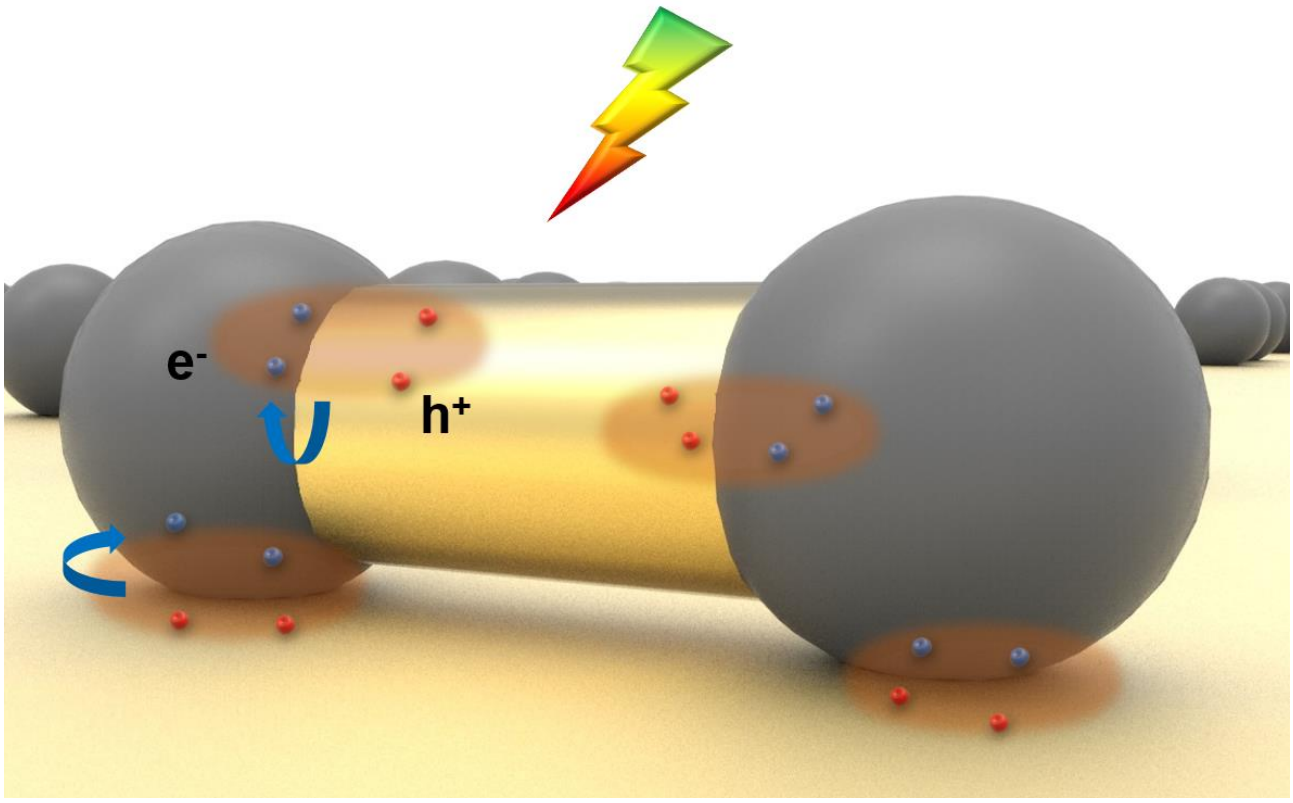

Table of content: In this study we presents the Au/TiO_2 dumbbell on Au film nanocavity system. This system is featured with a dual hot electron injection channels recognized as the efficient localized plasmon resonance mechanism and the d band optical transition mechanism.

Supporting Information

Title: Plasmonic Au/TiO2-dumbbell-on-film nanocavities for high-efficiency hot-carrier generation and extraction

*Kwun Hei Willis Ho, Aixue Shang, Fenghua Shi, Tsz Wing Lo, Pui Hong Yeung, Yat Sing Yu, Xuming Zhang, Kwok-yin Wong, Dang Yuan Lei**

S1. Statistics on the dimensions of Au nanorods and Au/TiO_2 nanoparticles:

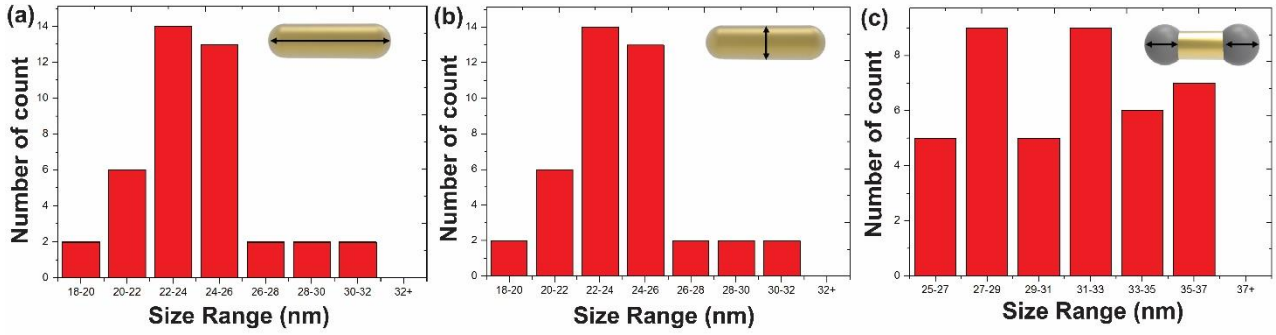

$\bar{x}$=77.8 nm $\bar{x}$=24.20 nm $\bar{x}$=31.1 nm

Figure S1. Histogram statistics of the physical dimensions of Au nanorods and Au/TiO_2 dumbbells: (a) the longitudinal length and (b) the diameter of the Au nanorods, and (c) the thickness of TiO_2 shells.

S2. Au/TiO_2 deposition by drop-casting and spin-coating

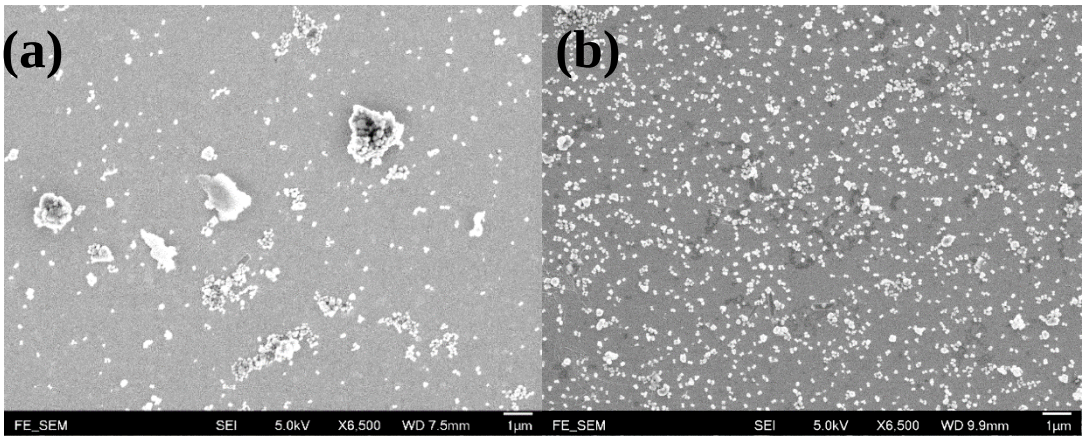

Figure S2. Au/TiO_2 dumbbell nanoparticles deposited on Au film with (a) drop-casting and (b) spin-coating.

S3. Schematic band diagram of a Au/TiO_2/ITO system

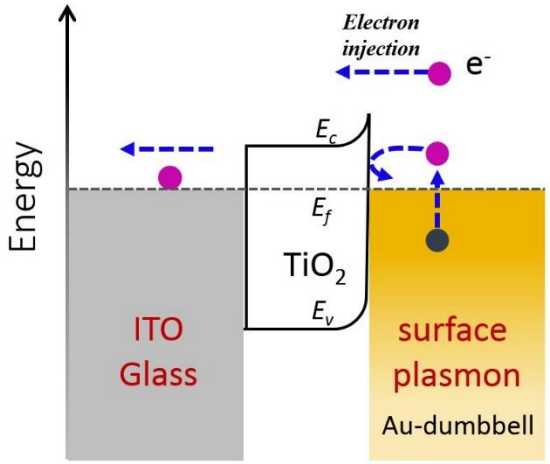

S4. Extinction spectra of Au/TiO_2 dumbbell nanoparticles on ITO substrate and Au film

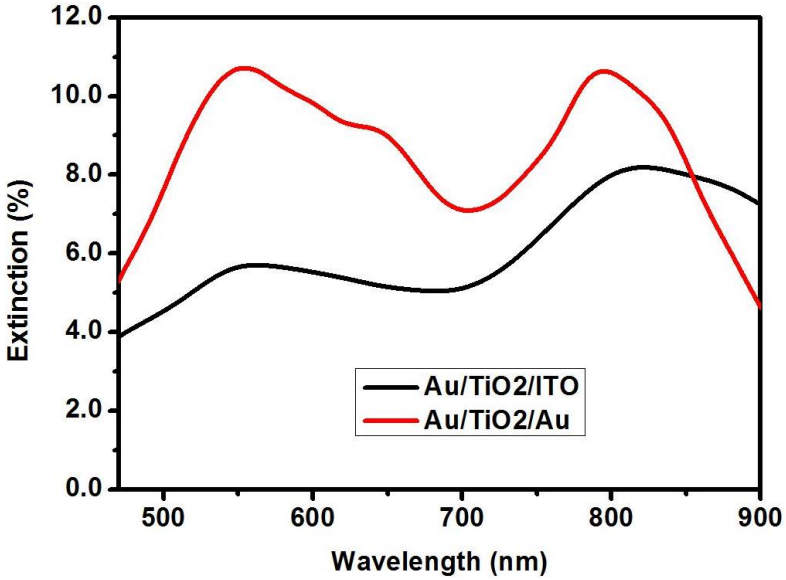

Figure S4. Measured extinction spectra of Au/TiO_2 dumbbells on an ITO glass (black) and on a thin Au film (red) using a microscope system equipped with a 50X objective.

S5. Reflectance of the Au/TiO_2/Au system and a bare Au film

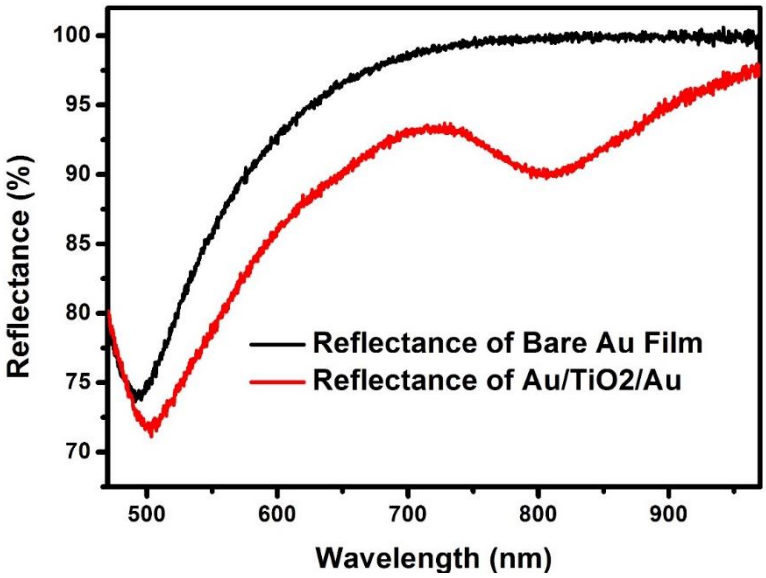

Figure S5. Measured reflectance spectra of the Au/TiO_2/Au system (red line) and a thin Au film (black line).

S6. Comparison of measured and FDTD-simulated extinction spectra

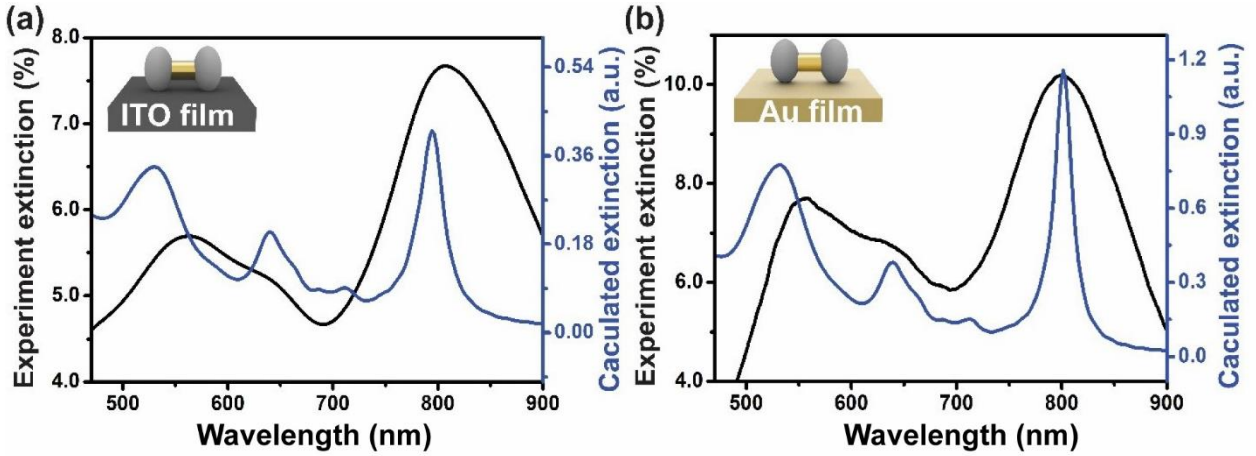

Figure S6. Comparison of FDTD-calculated extinction spectra (blue) and experimental extinction spectra obtained with a 10 X objective (black) for the Au/TiO_2/ITO system (a) and the Au/TiO_2/Au system (b).

S7. Photocurrent for the TiO_2/Au system and a bare Au film

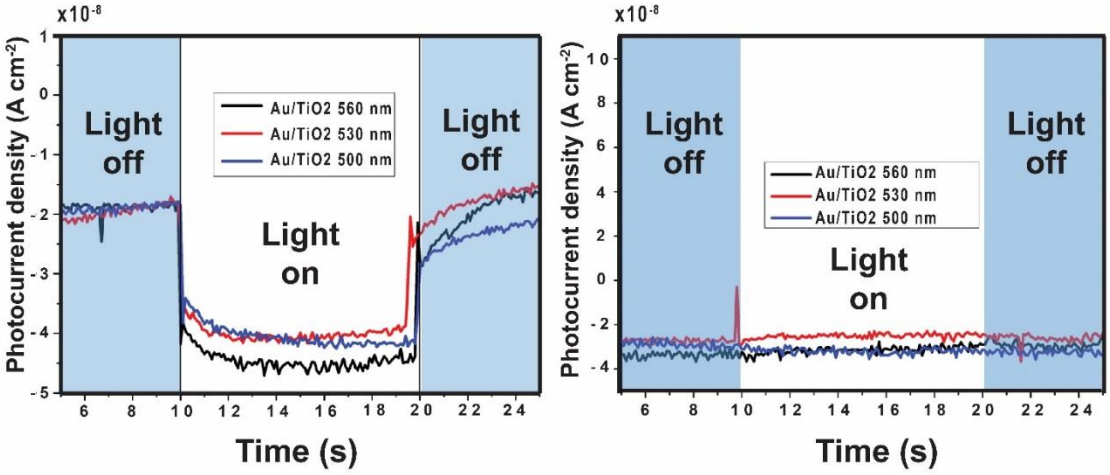

Figure S7. Measured photocurrent for a TiO2/Au system (a) and a bare Au film (b) under illumination with monochromatic light at the same condition as described in Experiment Section.

S8. Particle density inspection after MB decomposition experiment

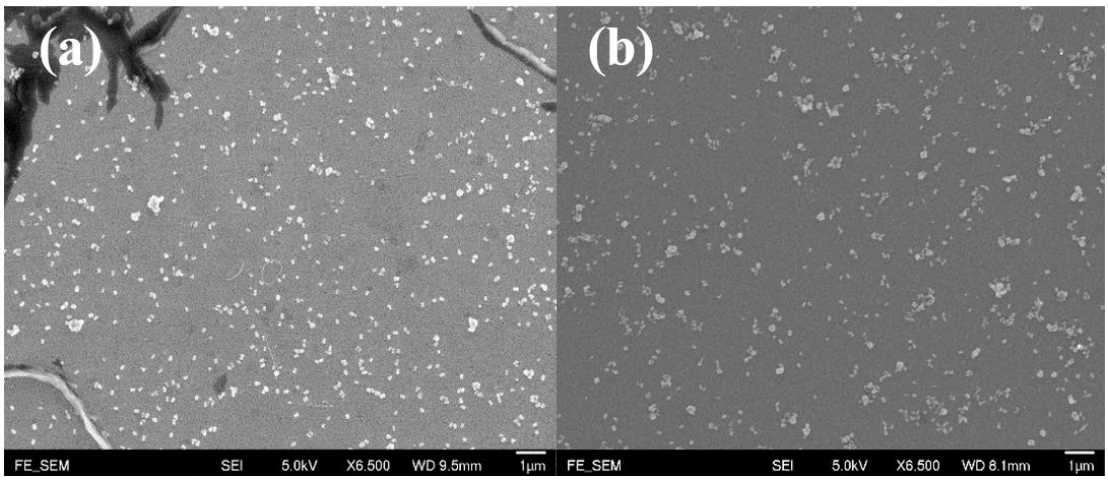

Figure S8. SEM images of Au/TiO_2 dumbbells on a thin Au film (a) and on an ITO glass (b), both captured after the MB decomposition experiment with flow rate of 10 μL min^{-1}.

S9. Redox partial reactions on working electrode (WE) and counter electrode (CE)

Photoanode: Au/TiO_2/ITO and Au/TiO_2/Au plasmonic systems

Methanol (CH_3OH) is oxidized by holes (h^+) generated on the Au nanorod surafce. The reaction follows the following pathway:

$$h^+ + CH_3OH + H_2O \rightarrow CO_2 + 6H^+ + 6e^-$$

Photocathode: Pt plate

Protons are reduced by electons in the following pathway:

$$e^- + H^+ \rightarrow H_2$$

S10. Illumination spectrum-dependent MB decomposition rate

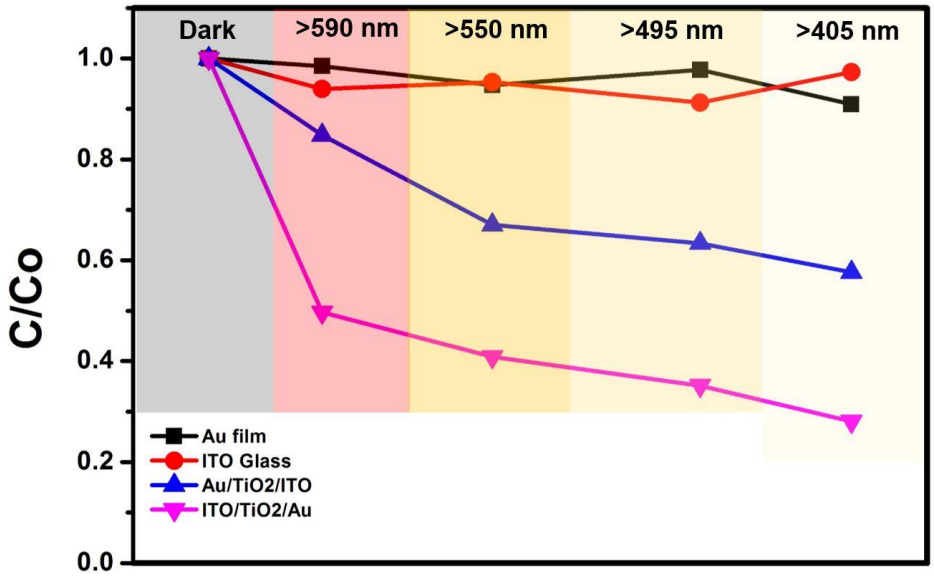

Figure S10. Measured illumination spectra-dependent MB decomposition rate. The black and red curves are the measured decomposition rates for a bare ITO and a bare Au film, respectively. The blue and magenta lines are the results for the Au/TiO_2 dumbbells on an ITO glass and on a thin Au film, respectively. All measurements were conducted at a constant flow rate of 10 μL min^{-1}.

S11. Action spectra of MB decomposition

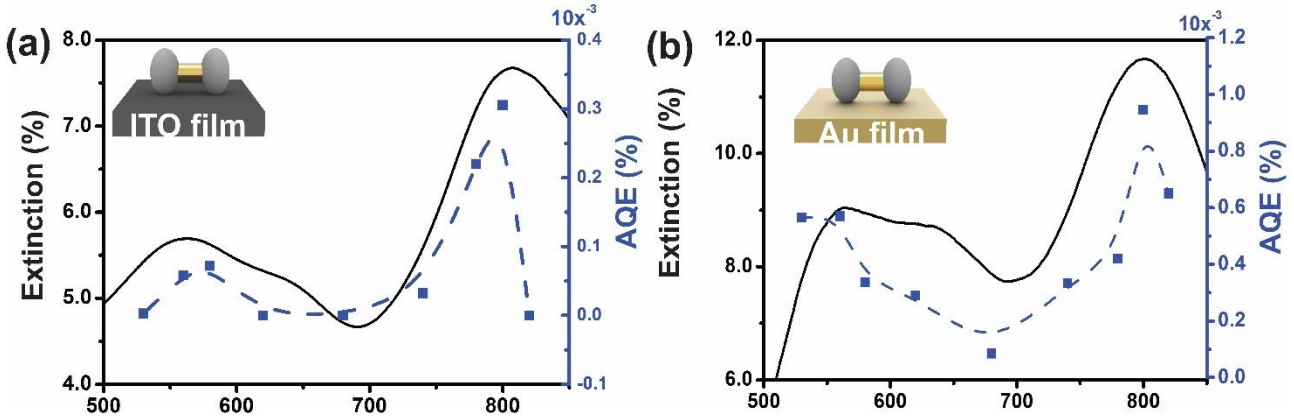

Figure S11. Comparison between action spectra and extinction spectra (obtained with a 10X objective) for the $Au/TiO_2/ITO$ system (a) and the $Au/TiO_2/Au$ system (b). The flow rate was kept at constant of 10 μL min^{-1}.